Metal-insulator crossover in monolayer MoS 2

I Castillo, T Sohier, M Paillet, D Cakiroglu, C Consejo, C Wen, F Wasem Klein, M.-Q Zhao, A Ouerghi, S Contreras, et al.

Metal-insulator crossover in monolayer MoS_2

I. Castillo,[1] T. Sohier,[1,2] M. Paillet,[1] D. Cakiroglu,[1,3] C. Consejo,[1] C. Wen,[4] F. Wasem Klein,[1] M.-Q. Zhao,[5,6] A. Ouerghi,[7] S. Contreras,[1] A.T. Charlie Johnson,[6] M. J. Verstraete,[2] B. Jouault,[1] and S. Nanot[1]

[1] *Laboratoire Charles Coulomb (L2C), UMR 5221 CNRS-Université de Montpellier, Montpellier, France.*
[2] *Nanomat/QMAT/CESAM, University of Liège, Belgium*
[3] *Engineered Nanosystems Group, Department of Neuroscience and Biomedical Engineering, School of Science, Aalto University, Aalto, Finland*
[4] *Department of Electrical and Systems Engineering, University of Pennsylvania, Philadelphia PA 19104, USA.*
[5] *Otto H. York Department of Chemical and Materials Engineering, New Jersey Institute of Technology, Newark, New Jersey, 07103, USA.*
[6] *Department of Physics and Astronomy, University of Pennsylvania, Philadelphia PA 19104.*
[7] *Centre de Nanosciences et de Nanotechnologies (C2N), Université Paris-Saclay, France*

We report on transport measurements in monolayer MoS_2 devices, close to the bottom of the conduction band edge. We have developed a method to anneal *in situ* MoS_2 devices before electrical measurements. This allows us to obtain good ohmic contacts at low temperatures, and to measure precisely the conductivity and mobility *via* four-probe measurements. The measured effective mobility up to $\mu_{\text{eff}} = 180$ cm^2/Vs is among the largest obtained in CVD-grown MoS_2 monolayer devices. These measurements show that electronic transport is of the insulating type for $\sigma \leq 1.4e^2/h$ and $n \leq 1.7 \times 10^{12}$ cm^{-2}, and a crossover to a metallic regime is observed above those values. In the insulating regime, thermally activated transport dominates at high temperature ($T > 100$ K). At lower temperatures, conductivity is driven by Efros-Schklovkii variable range hopping in all measured devices, with a universal and constant hopping prefactor, that is a clear indication that hopping is not phonon-mediated. At higher carrier density, and high temperature, the conductivity is well modeled by the Boltzmann equation for a non-interacting Fermi gas, taking into account both phonon and impurity scatterings. Finally, even if this apparent metal-insulator transition can be explained by phonon-related phenomena at high temperature, the possibility of a genuine 2D MIT cannot be ruled out, as we can observe a clear power-law diverging localization length close to the transition, and a one-parameter scaling can be realized.

I. INTRODUCTION

Following the keen interest in 2D materials started with graphene, transition metal dichalcogenides (TMDs) have been among the first ones to be intensely studied during the past ten years.[1] Molybdenum disulfide (MoS_2) has been the most studied TMD so far. The most remarkable properties of MoS_2 monolayers are their large direct band gap (1.8 eV[2–5]), their strong spin-orbit coupling which qualify them for numerous photonic applications, and their excellent mechanical properties which makes them a compelling semiconducting material for flexible electronics.[6,7]

In particular, field-effect-transistors based on monolayer MoS_2 were found to exhibit high on/off ratios, steep sub-threshold swing, with reported electron effective mobility ranging from 1 to 480 cm^2/Vs.[8–16] These mobilities are already high enough to present MoS_2 monolayers as an alternative to traditional organic material or amorphous silicon for low-end applications, for example, high resolution displays and photodetection.

Most of the initial studies were performed on exfoliated MoS_2 flakes, a process of great versatility but unfortunately not scalable at an industrial level. A significant advance was realized with the production of MoS_2 by Chemical Vapor Deposition (CVD), down to the monolayer. Such a process paved the way towards commercially viable MoS_2-based devices, at affordable costs and with good reproducibility.

In the experimental studies realized on CVD MoS_2, the mobility did not exceed 80 cm^2/Vs,[9,11,17] a value lower than the one predicted theoretically,[18] and lower than those measured in exfoliated MoS_2. This mobility degradation has been attributed to the presence of charged states at the interfaces with the dielectric layer,[11] but also to structural defects like vacancies,[19] and the presence of large band-tails in the gap.[9]

As noted in by Zhu *et al.*,[9] there are technical difficulties in accurately measuring mobility in such devices. The main problems are due to the inhomogeneity of MoS_2 and the high contact resistances - which severely limits the potential use of two-probe measurements. The most appropriate technique is based on four-probe measurements, combined with a measurement of the so-called "drift mobility".[16,20] Hall mobility, which can only be determined by additional Hall measurements, has only worked well at very high doping.[16,21,22]

Because of all these technical issues, Only a few detailed studies have been performed so far.[8,11] The understanding of the basic transport properties of these CVD-grown MoS_2 devices still calls for additional experiments, which could also reveal some rich physics. In particular, it was evidenced that at the bottom of the MoS2 conduction band, a true two-dimensional insulator transition can take place.[23–25]

Here, we present a systematic study of the electronic properties of scalable CVD MoS_2 monolayers. Thanks to *in-situ* annealing, we could perform a systematic 4-probe analysis, as a function of temperature and gate voltage, and report mobilities as high as 180 cm^2/Vs. These experiments also confirm the presence of a sizable band tail at the bottom of the conduction band, which has a deep impact on the electrical device performance. We mainly focused on the low electron density regime where the devices exhibit an insulating behavior (the conductivity increases when the temperature increases). There, at low temperatures, below ∼150 K, the band tail induces variable range hopping from which the localization parameters can be extracted. Then, as the temperature progressively increases, thermal activation takes place. However, at high enough carrier densities the devices exhibit a metallic behavior (the conductivity decreases when the temperature increases). In this last regime, complementary modeling allows us to draw insights into the relative influence on the mobility of impurity and phonon scatterings. Finally, we also briefly discuss the relevance of a genuine quantum transition model proposed in previous works[23–25] to explain the crossover between these two behaviors at low temperature.

II. DEVICE FABRICATION AND CHARACTERIZATION

A. Growth and fabrication

Thin MoS_2 (mostly monolayer) flakes were grown by Chemical Vapor Deposition (CVD) on ∼ 300 nm of SiO_2 on top of a heavily doped Si substrate. First, the precursor, a mixed aqueous solution of 1.5×10^{-3} M ammonium heptamolybdate (AHM) and 0.2 M NaCl, was spin-coated at 3000 rpm for 60 s onto the SiO_2/Si substrate. After that, the substrate was placed in the center of a 1 in. CVD tube furnace and 30 mg of sulphur was placed 20 cm upstream from the substrate. The furnace temperature was ramped to 750 °C at a rate of 70 °C.min^{-1} under a flow of 400 sccm of Argon gas (99.99% purity) and kept at 750 °C for 5 min. While the SiO_2/Si growth substrate reached 750 °C, the maximum temperature of the sulphur was ≃ 150 °C. After the growth, the furnace was opened, and the sample was rapidly cooled to room temperature in 400 sccm flowing Argon.

Monolayer flakes were then identified by optical contrast and confirmed with Raman and reflectometry measurements. Selected MoS_2 flakes were shaped into Hall bars using electron beam lithography (EBL) and reactive ion etching (20 W RF power for 5 min. with CHF_3 (60 sccm), O_2 (20 sccm) and Ar (10 sccm)) and top-contacted with a titanium adhesion layer and gold. 11 devices have been measured and, in the following, we present the most detailed results obtained in three devices, named M1, M2 (from the same growth and process with 330 nm of SiO_2 on top of *n*-doped Si and Ti(2 nm)/Au(150 nm) contacts) and M3 (from a different growth on *p*-doped Si/SiO_2(288 nm) and Ti(15 nm)/Au(75 nm)). Optical pictures of these devices are available in the Supp. Info.

A colored scanning electron micrograph after processing is shown in Fig. 1(a). The typical triangular shape of CVD MoS_2 is still well visible, even after the contact deposition, with the MoS_2/metal contact area being maximized in order to minimize the contact resistances.

B. Raman analysis

A complete and detailed Raman mapping of the devices M1 and M3 was performed after the electrical measurements to assess the homogeneity and quality of the devices. These measurements were realized with an optical wavelength of 532 nm and a spot size ∼0.5 μm, allowing a complete spatial mapping of the devices.

Figure 1(b) shows the average Raman spectra obtained in devices M1 and M3. An additional sample, obtained by exfoliation of a MoS_2 monolayer, is also shown for comparison. The Raman modes A_{1g} and E^1_{2g} exhibit sensitive thickness dependence, which provides a convenient mean for determining the number of MoS_2 layers (Fig. 1b).[26] These two modes are centered around 385 cm^{-1} and 405 cm^{-1} respectively, which are typical values for monolayer flakes on SiO_2.[26] Further analysis can be obtained from the frequency difference $\delta = \omega(A_{1g}) - \omega(E^1_{2g})$. In device M1, δ is very homogeneous over the entire MoS_2 surface. It is centered around 20 cm^{-1}, with a variation of less than 0.8 cm^{-1}, as shown in the colormap as a function of position and in the full width at half maximum of the histogram distribution (Fig. 1c). This low δ value associated with its narrow distribution are the signature of a homogeneous MoS_2 monolayer. Similar results were obtained with device M3, where, however, a few small additional MoS_2 bilayer patches were also evidenced but representing less than 1% of the total surface. These patches were also visible in optical and SEM images, confirming their very low percentage (not shown here).

Figure 1(d) evidences the presence of additional modes at lower frequencies. Among these modes, the $LA(M)$ peak around 227 cm^{-1} is of particular interest since it was attributed to disorder-induced Raman scattering.[27] Its intensity is proportional to the density of defects n_D. Following Mignuzzi *et al.*,[28] the average inter-defect distance L_D can be evaluated from the ratio $\mathcal{R}$ of the peak intensities of the $LA(M)$ and A_{1g} mode. Device M1, with $\mathcal{R} \sim 0.044$ (L_D = 3–4 nm, n_D = 1.5–3 $\times 10^{12}$ cm^{-2} for a random defect distribution), hosts a typically large number of defects, wehereas, by comparison, device M3 appears to be less defective (below the detection limit of this approach with $\mathcal{R} < 0.005$, $L_D > 10$ nm, $n_D \leq 2.5 \times 10^{11}$ cm^{-2}).

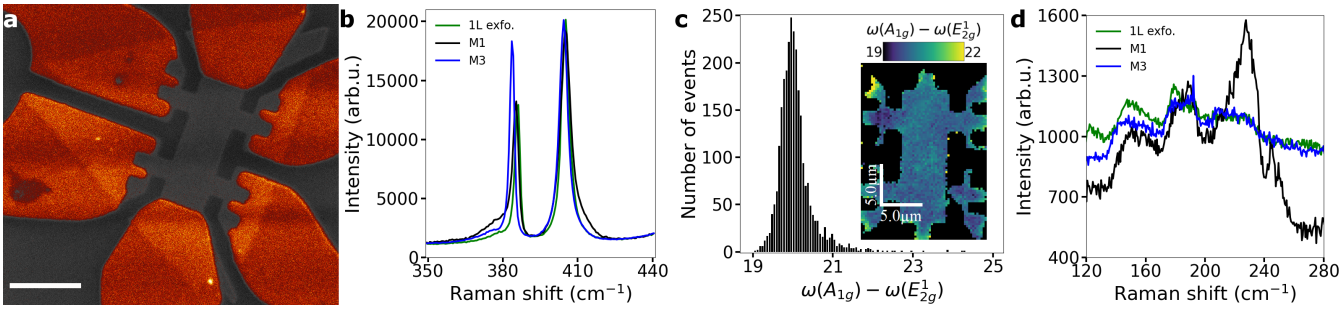

FIG. 1: (a) Secondary electron SEM image of a typical Hall bar device made from a MoS_2 flake (light gray region) and top contacted with a Ti/Au layer (in false red color). Scale bar is 10 μm.(b) Average Raman spectra of devices M1, M3, and an exfoliated monolayer MoS_2 reference around 400 cm^{-1}. The black, blue and green lines correspond to device M1, device M3, and an exfoliated MoS_2 monolayer reference respectively. The 3 spectra exhibit two peaks due to to the E^1_{2g} mode at $\simeq$ 384 cm^{-1} and the A_{1g} mode at $\simeq$ 405 cm^{-1}. (c) Histogram of the frequency difference $\omega(A_{1g}) - \omega(E^1_{2G})$ of device M1, extracted from the map analysis shown in inset. *Inset:* Color map of the frequency difference δ along the surface of device M1. (d) Low frequency Raman spectra showing the LA mode around 227 cm^{-1} . The same color reference has been used as in (b). The Si spectrum backround has been subtracted subtracted.

C. Preliminary electrical characterization and annealing

Electrical measurements were performed in a closed-cycle helium cryostat with heating capabilities up 1100 K, under primary vacuum. The DC two-terminal and four-terminal $I-V$ characteristics were recorded as a function backgate voltage at different temperatures.

After fabrication, all measured devices exhibited high, non-linear resistances above 1 GΩ and the electron conduction was merely accessible at high positive gate voltages. To reduce the electrical resistance, the devices were annealed at 600 K in vacuum ($\sim 10^{-3}$ mbar) before measurements. Devices M1, M2 and M3 have been annealed during 4 min., 11 min. and 15 min. respectively. It is worth noting that M2 has been annealed a second time for 26 min. without any noticeable change in all the results presented here (see Supp. Info.). The measurements were then performed starting at 500 K down to 20 K without any further exposure to air (in vacuum down to 300 K and in low pressure He gas below 300 K).

After annealing, the two-probe resistance dropped down below the MΩ range and became comparable to the four-probe resistance (Fig. 2). Such an increase in contact transparency by *in-situ* annealing was also observed in WS_2.[29] The consistency and reliability of the four-probe measurements was checked at each temperature by measuring the two-probe, $I_{sd}(V_{sd})$, and four-probe, $I_{sd}(V_x)$, current-voltage characteristics at fixed backgate voltages, V_g. These measurements are illustrated in Figure 2 for two devices at $V_g = 100$ V. Whereas the two-probe curves are not systematically perfectly linear, the four-probe curves are linear in the whole temperature range analyzed in this work. Thus, the $I_{sd}(V_{sd})$ non-linearity is induced in the vicinity of the contacts in this V_{sd} range. Electrical contacts are commonly of Schottky type in top-contacted MoS_2 with metals.[14,30,31] As the I_{sd} current is limited by the blocking Schottky contact, the superlinear behavior may be due to image force, or tunneling. A thorough study of the contact resistance will be presented elsewhere.

This annealing also considerably doped the MoS_2 with n-type carriers, shifting the threshold voltage, V_{Th}, defined in the next chapter, by $\sim$ 120 V towards negative values (see Supp. Info.). This increase in doping with annealing has already been documented.[11,12,16] It can be explained by the desorbtion of molecules in the vicinity of MoS_2, and in particular, near sulfur vacancies which will then act as electron donors.[2] This results in a large increase of both carrier density and conductivity.

Finally the gate dependent conductivity curves exhibited hysteresis at high temperatures for temperatures above $\sim$350 K.[32–34] The amplitude of the hysteresis decreases with temperature and there is no hysteresis for T $\leq$ 300 K (see Supp. Info.). These observations are consistent with the presence of oxide traps at the Si/SiO_2 interface and possibly mobile ions close to the SiO_2/MoS_2 interface.[32–34] A typical hysteresis (at 400 K) for our devices is $\Delta V_T \sim 10-20$ V, which allows us to estimate a lower value for the doping inhomogeneity of $N_T \gtrsim 10^{12}$ cm^{-2}, using a simple capacitive model: $N_T > \Delta N_T \geqslant \Delta V_T \cdot C_{ox}/e$, where C_{ox}= 1.04 $\times$ 10^{-8} F/cm^{-2} is the geometric capacitance. We could also note that the hysteresis loop is anti-clockwise, which is not consistent with MoS_2 traps or defects. So, the N_T value is not related to the intrinsic defect density given by the Raman analysis, but rather with charge traps in the SiO_2 substrate, as discussed in section IV.A.

III. RESULTS: TEMPERATURE DEPENDENT CONDUCTIVITY

In the following, we will study the conductivity σ of these MoS_2 devices as a function of backgate voltage, V_g, at different temperatures, T. All those results have

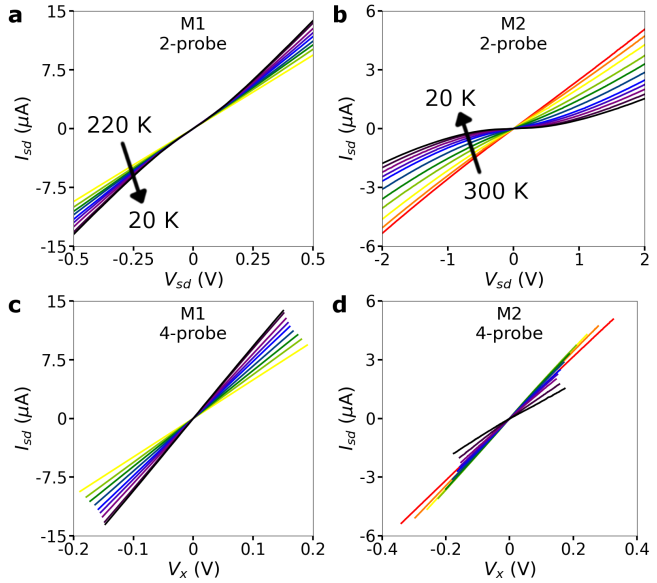

FIG. 2: (a) (and (b)) Two-probe and (c) (and (d) four-probe current voltage characteristics for M1 (respectively, M2) at $V_g = 100$ V between 220 K and 20 K (300 K and 20 K, resp.). I_{sd} is the current flowing through the device from source to drain, V_{sd} is the voltage between source and drain, and V_x is the voltage measured in the four probe configuration. These contacts are explicitly labeled in the devices figures in the Supp. Info.

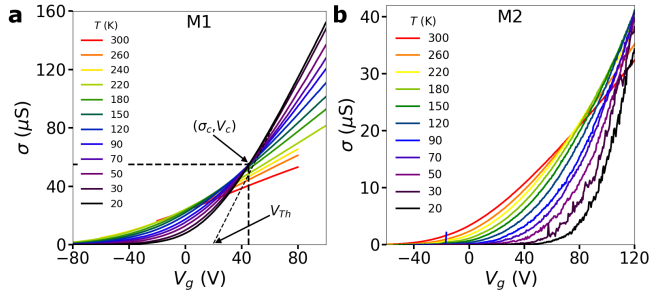

FIG. 3: Four probe conductivity of devices (a) M1 and (b) M2 as a function of gate voltage, at different temperatures from 20 K to 300 K.

been obtained in domains in which the $I_{sd}(V_x)$ curves are linear and the gate hysteresis is negligible, to ensure that the resistivity of the MoS_2 is extracted correctly. Depending on the devices (more precisely their conductivity and doping), an insulating or metallic temperature dependence is observed. After presenting these main results, we will briefly discuss how this crossover matches the disorder estimated in section II, and we will evaluate the expected Coulomb interaction in order to assess properly the transport mechanisms in the analysis section.

A. Conductivity : Metallic and insulating behavior

Figure 3 shows the conductivity $\sigma(V_g, T)$ of devices M1 and M2. For M1 (Fig. 3a), the conductivity is vanishingly small at $V_g = -80$ V, and steadily increases with V_g. This unipolar gate dependence is typical of MoS_2-based transistors (see *e.g.*[8,10,11,16]). It corresponds to an increase of electron doping (carrier density) and the progressive onset of current flowing through the conduction band. A qualitatively similar V_g dependence is observed for M2 (see Fig. 3b) .

At $V_g < 0$ V, the conductance decreases with T, indicating a clear insulating behavior. At the opposite, for $V_g > 45$ V, the conductance decreases with increasing temperatures, indicating a metallic behavior. The crossover between the two regimes can be associated to a crossing point between two $\sigma(V_g)$ curves taken at close temperatures. In the temperature range $T = 20 - 120$ K, the crossing point marking the transition is remarkably temperature-independent and is located at $V_g = V_C \simeq 45$ V and occurs at $\sigma = \sigma_c = 55\ \mu S \simeq 1.4e^2/h$. Above 120 K, the crossing point shifts slowly down to $V_g \simeq 0$ V at $T = 300$ K. For device M2, a clear insulating behavior is observed for $V_g < 80$ V, and the crossover to a metallic regime starts to be visible at $V_g = V_C \simeq 120$ V below 120 K (and also shifts to a lower gate voltage, $V_g \simeq 80$ V at $T = 300$ K). Device M3 conductivity is much less gate-dependent and only a metallic temperature dependence could be observed with $\sigma \in [100, 700]\mu S > e^2/h$ (presented in the Supp. Info. and Fig. 7d). This can be understood by the fact that it was considerably more doped than M1 and M2 after the annealing process.

This apparent two-dimensional metal-insulator transition (2D MIT) was first observed in MoS_2 monolayer by Radisavlevic and Kis,[8] and later by Baugher *et al.*,[16] Schmidt *et al.*,[11] Yu *et al.*[10] and more recently by Moon *et al.*[23–25] The experimental ubiquity of this MIT, systematically observed with a critical conductivity around e^2/h in various samples, has not been elucidated yet. It was suggested that this phenomenon originates from percolation,[35] as already observed in two dimensional electron gases,[36] or from a genuine 2D MIT induced by interactions.[23–25] It should also be noted that the term MIT is sometimes used to refer to scattering dependent mechanisms.[10,11,37] In this case, the crossover between a metallic and insulating behavior is due to a transition between impurity and phonon dominated scattering.

B. Introducing crossover

The scaling theory of localization by Abrahams predicts that a non-interacting 2D electron gas is always an insulator,[38] has no mobility edge, and cannot have a genuine 2D MIT. In this line of thought, the Ioffe-Regel criterion for the wave localization in disordered media stipulates that an Anderson phase crossover from weak to strong localization[39] occurs in a 2D gas when $k_F l_e \simeq 1$.

Here, $k_F = \sqrt{2\pi n_{2D}}$ is the wavevector at the Fermi energy, n_{2D} is the electron concentration, $l_e = \hbar k_F \sigma / n_{2D} e^2$ is the mean free path of the electrons and $-e$ is the electron charge. In two dimensions, neglecting screening, the Ioffe-Regel criterion gives an expected conductivity $\sigma_{c,IR}$ at the crossover independent of the charge concentration:

$$\sigma_{c,IR} = \frac{g_s g_v}{2} \frac{e^2}{h}, \tag{1}$$

where g_s and g_v are the spin and valley degeneracies respectively. For MoS_2, $g_s = 2$ and $g_v = 2$, thus $\sigma_{c,IR} = 2e^2/h \simeq 80\ \mu$S.

The experimentally observed $\sigma_c \simeq 1.4e^2/h$ is reasonnably close to $\sigma_{c,IR}$. Besides, the carrier density is given by $n_{2D} = C_{ox}(V_g - V_{Th})$. At $T = 20$ K, V_{Th} can be extrapolated from the linear part of the conductivity at high gate voltage (see Fig. 3). We get $V_{Th} \simeq 18$ V (and $V_{Th} \simeq 87 \pm 6$ V) for device M1 (and M2, respectively). The crossover charge density is then estimated at $n_c \simeq 27 \times C_{ox}/e \simeq 1.7 \times 10^{12}$ cm^{-2} for both devices M1 and M2. This yields $l_e \simeq 3$ nm at the crossover, or "2D MIT". These values are quite close to the defect density deduced from the Raman LA(M) peak intensity of device M1, as well as the susbstrate induced doping inhomogeneity (estimated from the high temperature gate hysteresis).

C. Introducing electron interactions

Interactions are strong in monolayer MoS_2 and cannot be neglected *a priori*. Usually, the correlation between carriers is measured via the dimensionless interaction parameter r_s which is the ratio between the Coulomb energy E_C and the kinetic energy E_F:

$$r_s = \frac{E_C}{E_F} = \frac{g_v}{a_B^* \sqrt{\pi n_{2D}}} = m^* e^2 g_v / 4\pi\epsilon\epsilon_0 \hbar^2 \sqrt{\pi n_{2D}}$$

where $a_B^* = (4\pi\epsilon\epsilon_0)/(m^* e^2)$ is the effective Bohr radius, $m^* = 0.45$ is the effective electron mass,[40,41] ϵ_0 the vacuum dielectric constant, and ϵ_r is the relative dielectric constant of the system which we evaluate by the Keldysh formula:[42] $\epsilon_r \simeq (\epsilon_r(SiO_2) + \epsilon_r(\text{air}))/2 \simeq 2.5$. This gives $r_s \simeq 20$. If we use the value $\epsilon_r = 7.3$ calculated for monolayer MoS_2,[43] we still get $r_s \simeq 8$. In both cases, such a ratio ($r_s \gg 1$) points toward the fact that electron-electron interactions cannot be neglegted to describe transport mechanisms occuring in MoS_2.[8,23]

IV. ANALYSIS: TRANSPORT MECHANISMS

In this section, we will discuss how this transition or crossover is well reproduced by semi-classical models at high temperature: thermal activation in the insulating regime and phonon scattering in the metallic one; while, at low temperture (below $T \simeq 120$ K), variable-range hopping (VRH) and impurity scattering dominate the insulating and metallic transport respectively. We will first discuss the insulating regime from thermal activation to VRH. Then, we will use the strong correlation implied by our analysis to test a model consistent with a phase transition and its limitation. Finally, we will discuss how the metallic regime is well described by a more standard single particle model when phonon and impurity scattering are at play.

A. Thermal activation at high temperature

The conductivity of device M1 is reploted in Figure 4a as a function of $100/T$. Thermally activated transport is given by a simple exponential law $\sigma \propto \exp(-E_a/k_B T)$ where E_a is an activation energy.[2,9,44] While the data at low temperatures and in the metallic region cannot be fitted by this model, the high-temperature part of the insulating region (above 100 K) seems to follow such an activation law below the threshold voltage $V_{Th} = 18\ V$. This approach is further justified by the dimensionless energy analysis detailed in the next section (see Fig. 4b). Assuming that E_a corresponds to the energy needed for an electron in an (impurity) in-gap state to be thermally excited in the conduction band, we then get $E_a = E_c - E_F$, where E_F is the Fermi energy and E_c the energy at the bottom of the conduction band. From a capacitive model accounting for the geometric capacitance, C_{ox} and the gate induced shift in E_F, we get the relation:[44]

$$-\frac{dE_a}{dV_g} = \frac{dE_F}{dV_g} = \frac{eC_{ox}}{C_{ox} + C_q}, \tag{2}$$

where $C_q = e^2 N(E_F)$ is the quantum capacitance and $N(E)$ is the density of states (DoS) at the energy E.

From these fittings of $\sigma(T)$ curve (Fig. 4a), one gets $E_a(V_g)$, which in turns allows us to reconstruct the DoS, $N(V_g)$ or $N(E_a)$ (Fig. 5). We find that $E_a \to 0$ when $V_g \to V_{Th}$ and $N(V_g = V_{th}) \sim 3 \times 10^{14}$ eV^{-1}cm^{-2}, which is the value expected for a parabolic band with an effective mass $m^* = 0.45\ m_0$.[40,41] This makes us confident that above 100 K the temperature dependence of the conductivity indeed corresponds to the thermal activation from localized states to the bottom of the conduction band. We can then extract the shape of the band tail below E_c (*i.e.* below V_{th}) using $N(E - E_c) = N(E = E_c) \times \exp((E - E_c)/s) + N_0$ (Fig. 5b).[9] The DoS decreases exponentially on a typical energy scale $s \sim 25$ meV, and an energy independent impurity DoS $N_0 \sim 10^{13}$ eV^{-1}cm^{-2} is included in the fitting.

Nearest neighbor hopping could also play a role, especially for very high activation energies (which would account for the need to introduce a rather high N_0 to fit these results), Nevertheless, this exponential decay is consistent with the spatial doping fluctuations encountered in 2D materials on SiO_2 substrates.[45] Using $s \sim 25$ meV, the expected integrated density of localized

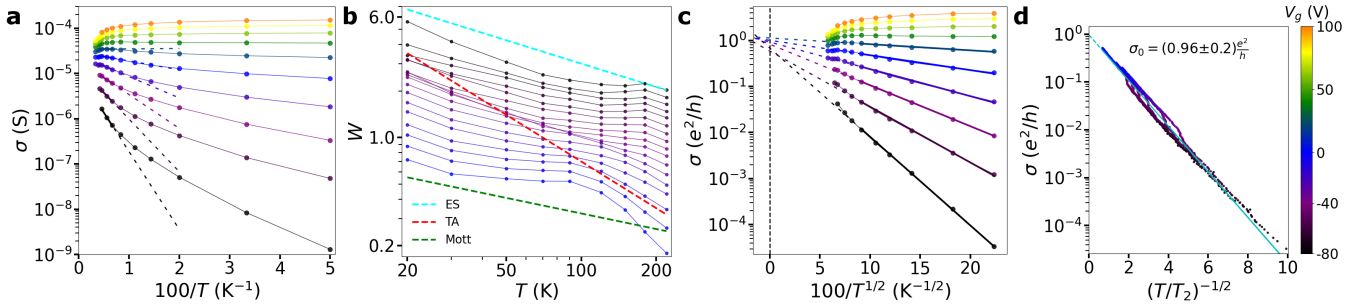

FIG. 4: (a) Four-probe conductivity σ of device M1, as a function of $100/T$, at different gate voltages between -80 V and 100 V (black to orange curves). (b) Temperature dependence of the dimensionless energy activation $W = T^{-1}\partial \ln \rho(T)/\partial T^{-1}$ on a logarithmic plot, for gate voltages varying between -80 V and 0 V. The dashed lines correspond to the expected $-1/p$ slope for different transport mechanims: thermally activated transport (TA) with p = 1, Efros-Shklovskii (ES) VRH with p = 2, and Mott VRH with p = 3 (see equation (3). (c) Temperature dependence of the conductivity versus $T^{-1/2}$. The data below $T = 100$ K and $V_g = 20$ V have been fitted by the black solid lines, the dashed lines are the extrapolation to $T^{-1/2} = 0$. (d) Conductivity σ in units of σ_0 as a function of $(T/T_2)^{-1/2}$. The best linear fit is indicated by a dashed blue line. The color scale is the same for all the subfigures and only a reduced data set is indicated for (a), (b) and (c) for clarity.

states is on the order of $N(s) \times s = 2.7 \times 10^{12}$ cm^{-2}. By comparison, we estimated a charge trap density $N_T \gtrsim 10^{12}$ cm^{-2} from the hysteresis at $T > 350$ K, in fair agreement with $N(s)$.

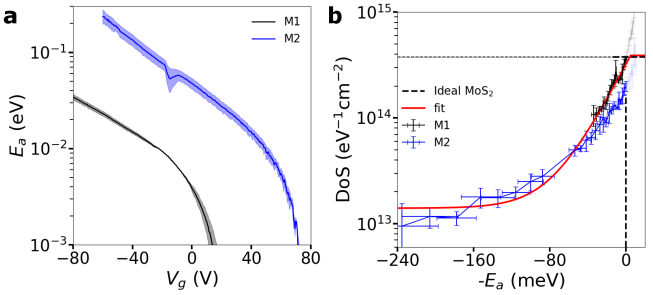

FIG. 5: (a) Activation energy as a function of gate voltage obtained from fitting the conductivity above 150 K with an exponential law. (b) Density of states as a function of activation energy computed using equation 2 and the results from panel a, where $E_a = -E_F$ and the bottom of the conduction band is at $E_a = 0$ meV.

B. Variable Range Hopping in the insulating region

At lower temperature, the conductivity tends to saturate. Usually, in disordered semiconductors, $\sigma(T)$ can be very well modeled in terms of VRH with the formula:[2,23,24,44]

$$\sigma = \sigma_0(T) \exp\left[-r_c/\xi\right] = \sigma_0(T) \exp\left[-\left(\frac{T_p}{T}\right)^{1/p}\right] \quad (3)$$

where σ_0 is a prefactor, r_c is the characteristic hopping length, ξ is the localization length, T_p and p are the characteristic temperature and exponent. The value of p depends on the exact form of the VRH mechanism. When electron-electron interactions can be neglected, the exponent is given by Mott's law and $p = 3$ in two dimensions. However, when screening is poor, Coulomb interactions must be included. In this case, the DoS is reduced in the vicinity of the Fermi energy. This corresponds to the Efros-Schklovskii (ES) VRH regime, and $p = 2$.

Previous studies in semiconductors unveiled two possible distinct behaviors for the prefactor σ_0. Several studies[46] revealed a temperature-dependent prefactor $\sigma_0 = AT^{-m}$, where $m = 1$ in the quantum Hall regime in GaAs/AlGaAs heterostructures,[47] or in graphene[46] or $m = 0.8$ in GaAs/AlGaAs quantum wells with or without magnetic field.[48] In other experiments, the zero-field 2D resistivity revealed ES VRH ($p = 2$), where the prefactor took a constant, universal value e^2/h. This remarkable universal prefactor was observed in Si metal-oxide semiconductor field-effect transistor,[49] in AlGaAs/GaAs heterostructure with a δ-doping situated very close to the interface,[50,51] and in insulating Si:B.[52] The temperature invariance of σ_0 implies that hopping in these systems is not mediated by phonons.[53] The possibility of variable-range hopping involving electron-electron interactions (instead of the usual electron-phonon mechanism) has been considered theoretically by a number of authors.[54–57] Interestingly, the importance of the prefactor $\sigma_0(T)$ and its temperature dependence has not been studied in monolayer MoS_2. In most experimental studies of TMDs thin films, a T-independent prefactor has been used.[2,23,44,58] In some others, $\sigma_0 \propto T^{-0.8}$ or $\sigma_0 \propto 1/T$ have been used to fit the conductivity,[13,45] without further justification. A closer look on σ_0 appears necessary to study the nature of the MIT.

To identify which VRH mechanism is at play in these results, we introduce the dimensionless energy $W = T^{-1}\partial \ln \rho(T)/\partial T^{-1}$. The slope of W on a logarithmic scale $\ln(W)$ *vs.* $\ln(T)$ gives directly the exponent p^{-1} of Eq. 3.[50] Figure 4b shows that for $V_g < -20$ V and $T < 100$ K, the value of p is very close to 2. By contrast,

$p = 3$ would give a too moderate slope, and the steeper slope for $p = 1$ indeed starts to appear at $T > 100$ K. Above $V_g = -20$ V, the slope decreases strongly, as already observed in n-doped germanium when approaching the metal-insulator transition.[59]

Assuming an ES VRH mechanism with the index $p = 2$, we can plot the logarithm of the conductivity as a function of $T^{-1/2}$, as shown in Figure 4c. As expected, the experimental data are very well fitted by straight lines over large domains of gate voltages and temperatures. The temperature coefficient T_2 is extracted from the fitting slope, and the prefactor σ_0 is given by the intersection of the fitting lines with the ordinate axis. All the lines intersect roughly at the same value of $\sigma_0 \sim 40$ μS, which regroup around the value e^2/h. Thus, σ_0 appears to be temperature independent. The universality of the prefactor is better seen in Figure 4d, where the conductivity in units of e^2/h is plotted as a function of $(T/T_2)^{-1/2}$, with T_2 extracted from the previous fitting (see Supp. Info.). All the data collapse onto the same straight line. A linear fit of these data confirms that the value of the prefactor is very close to e^2/h. The small residual discrepancy can be explained by a slightly incorrect geometric factor of the devices (width/length), for example.

For ES VRH, the localization length is related to the characteristic temperature T_2 by:

$$\xi = C_{ES} \frac{e^2}{4\pi\epsilon_r\epsilon_0 T_2} \tag{4}$$

where the prefactor $C_{ES} \simeq 6.2$ in two dimensions.[47] The relative dielectric constant ϵ_r has been approximated above as $\epsilon_r \simeq 2.5$. Figure 6a shows ξ as a function of the voltage difference $V_g - V_c$ (a complete plot of T_2 and ξ is shown in the Supp. info). This corresponds to very large values close to the metallic transition. If ϵ_r is constant as defined above, $\xi \sim 100$ μm at $V_g - V_c$= -10 V, and $\xi \sim 1$ mm at $V_g - V_c$= -4 V. These ξ values are unrealistically high, as they become larger than the sample size close to V_c. This discrepancy was already experimentally observed by Mason *et al.*[49] and Khondaker *et al.*.[51] It was suggested that the C_{ES} quoted above is too large by a factor of ten, as numerical calculations of a Coulomb glass with multielectron hopping gave a much lower value $C_{ES} \simeq 0.62$.[60] Keuls *et al.* also suggested a lower experimental limit of $C_{ES} = 0.64$.[48]

C. A genuine MIT?

Besides, Figure 6a shows that ξ (hence, T_2) has a clear power law behavior, suggesting that a second-order phase transition could be responsible for the apparent 2D MIT. In the theory of localization, ξ is expected to diverge close to the transition as $\xi \sim |n_{2D} - n_c|^{-\nu}$, where ν is called the correlation length exponent. Moon *et al.*[23–25] proposed to extend the Efros-Schklovskii VRH model close to the 2D MIT by using a phenomenological power law for the relative dielectric permittivity: $\epsilon \sim \xi^{\eta-1} \sim |n_{2D} - n_c|^{-\zeta}$.

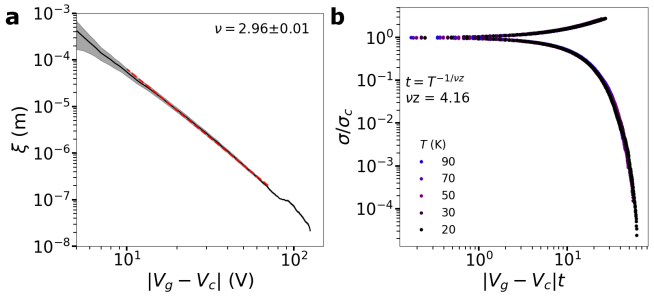

FIG. 6: (a) Localization length ξ as extracted from the ES VRH fit for M1 device. (b) σ/σ_c with respect to the rescaled gate voltage and temperature $|V_g - V_C|t \propto (n_{2D}/n_c - 1)T/T_0$ where $T_0(\delta n) \sim |\delta n|^{z\nu}$. See text for details.

Thus, $T_2 \sim \xi^{-\eta} \sim |n_{2D} - n_c|^{\eta\nu}$. Figure 6a shows the power-law behavior of ξ, which gives $\eta\nu \simeq 3$. If we assume an infinite sample size, the effective sample size L_{eff} is given by the phase coherence length which is associated with the temperature as $L_{\text{eff}} \sim T^{-1/z}$, z being the dynamical exponent. This relation leads to a one-parameter scaling law in the quantum critical region, which is represented by a simple mathematical form:

$$\sigma(T, \delta n) = \sigma_c \times f[T/T_0(\delta(n))],$$

where σ_c is the conductivity at n_c, f is a universal scaling function, $\delta_n = (n_{2D}/n_c - 1)$, and $T_0(\delta n) \sim |\delta n|^{z\nu}$. We choose the critical conductivity σ_c at $V_g = 45$ V. Following the theory, all experimental data should collapse onto a universal curve for each insulating and metallic phase after rescaling the temperature. Figure 6b shows indeed that such a scaling is possible. We restrict the analysis at temperatures lower than 90 K where the critical voltage V_c and conductivity σ_c are independent of the temperature. The scaling shown in Figure 6 has been done using a power law behavior for T_0 with $z\nu = 4.16$. We obtain the same $z\nu$ exponent for both sides of the transition, as expected from theory.

Thus, the data for device M1 are, in the limit of the available data, compatible with a 2D MIT. This observation is quite surprising since phonon contribution cannot be ruled out for this temperature range. Indeed, the Bloch-Grüneisen temperature[61] $T_{BG} \propto \sqrt{n}$ is on the order of the lowest experimental temperature at the critical point $T_{BG}(n_c) \simeq 24$ K (considering acoustic phonons). Unfortunately, a similar analysis could not be achieved with the other devices, as they are above, or below, the observed MIT. All the characteristic energy scales with regard to the experimentally observed transition are shown in more details in the Supp. Info. As a consequence, the existence of a 2D MIT should be crosschecked by additional measurements on other devices,[62] at lower temperatures, or as a function of electric field.[24]

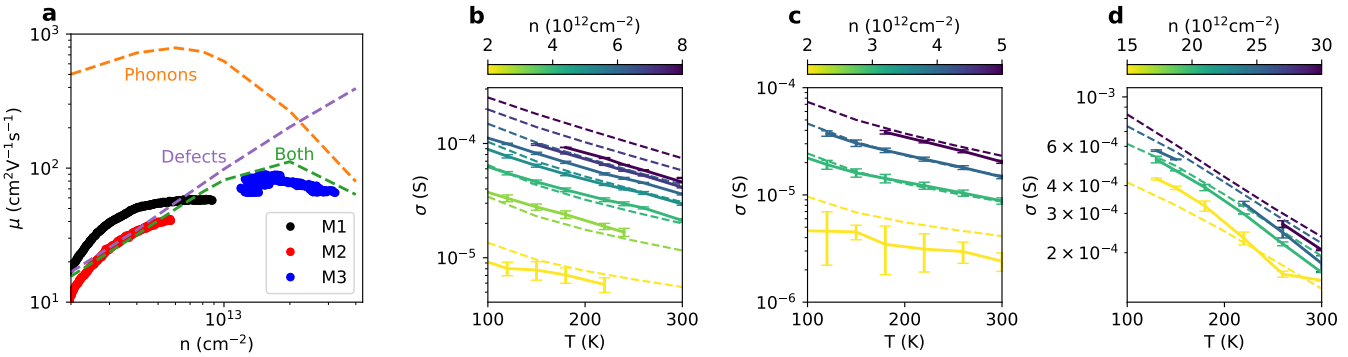

FIG. 7: (a) Mobility of the three devices M1 (black), M2 (red), and M3 (blue), at $T = 220$ K. The theoretical mobility is shown for phonon scattering only (orange), impurity scattering only with a defect density $n_D = 2.5 \times 10^{12}$ (purple line), and both scatterings (green). (b,c,d) Conductivity versus temperature for devices M1, M2 and M3 respectively, at different carrier concentrations. The experimental data are shown as solid lines; the best theoretical fits are indicated by dashed lines. The fitted point-charge defect densities are are $n_D = 1.7 \times 10^{12}$, 2.4×10^{12}, and 3×10^{12} cm^{-2} for devices M1, M2 and M3 respectively.

D. Metallic behavior: temperature dependent phonon and impurity scattering

In the following, we focus on the metallic part of the conductivity curves, at temperatures above 90 K and gate voltages above V_c. There, hopping is not at play, and we will show that the data are reasonably well reproduced by the usual single-particle model, when phonon and impurity scatterings are considered.

More precisely, the theoretical conductivity and mobility are simulated by considering electron scattering with phonons and point charge defects within a full energy- and momentum-dependent Boltzmann transport equation.[18,63] Electron-phonon interactions are computed *ab initio* using density functional perturbation theory.[64–66] As shown in a recent work,[63] the relative energy of the valleys in MoS_2's multi-valley electronic structure has a large impact on transport and density-functional theory values for this parameter should be taken with caution. Using the newly developed methodology of Ref.[63], the Q valley (halfway between Γ and K) can be shifted up or down in energy with respect to the bottom of the conduction band, at K. Long-range scattering from impurities is modelled via a density of point charges in the plane of the material, as it would be induced by common defects like charged sulfur vacancies in MoS_2.[67] Short-range, intervalley scattering from impurities was found to have smaller impact and was discarded to simplify the already complex transport model. Charge screening is included for both types of scattering, by computing the independent-particle static susceptibility (the response of the charge density to a potential perturbation).[63,68]

Thus, there are two unknown parameters in the simulations: the point charge density and the energy of the Q valley band edge. A close fit and reliably accurate values of both those parameters is quite challenging at this point, notably because the exact nature and quantity of impurities remains uncertain, and point-charge scattering is only an effective model. Our current aim is to obtain a reasonable fit with plausible choices for the parameters, showing that the main transport mechanisms can be understood within the present theoretical framework.

The Q valley is placed 90 meV above the K valley (at zero doping). This choice is based on matching the slope of the temperature-dependent conductivity and the approximate position of the peak in mobility versus carrier density. The impurity density is then tuned to best fit the data.

For this purpose, the experimental effective mobility is obtained as $\mu_{\text{eff}} = (\partial\sigma/\partial V_g)/C_{ox}$, and is shown in Figure 7a for the three devices, at $T = 220$ K. The electron concentration has then been estimated by $n_{\text{eff}} = \sigma/\mu_{\text{eff}}$. We tested that this approach gives a good agreement with a capacitive model using a temperature-dependent $V_{Th}(T)$ and $V_g > V_c$ (see Supp. Info. for more details). This confirms that the carrier density and band mobility can be confidently extracted even for M3, as long as $n_{\text{eff}} > 2 \times 10^{12}$ cm^{-2}, which is the case in the metallic regime.

The theoretical mobilities as a function of temperature are indicated for phonon scattering only, for impurity scattering only with a defect density $n_D \simeq 2.5 \times 10^{12}$ cm^{-2}, and accounting for both types of scattering together (Fig. 7a). Either type of scattering fails to fit the measurements: phonon scattering overestimates the mobility at low doping while defect scattering fails to reproduce the maximum in the density-dependent mobility. The increase of both phonon- and impurity-limited mobilities is due to the screening from the carriers added to the conduction band. The decrease of the phonon-limited mobility after $\sim 6 \times 10^{12}$ cm^{-2} is due to strong intervalley phonon scatterings being activated when the Fermi level approaches the Q valley. It appears from figure 7a that the combination of impurity and phonon scatterings

gives a fair fit of the mobility versus carrier concentration for the three studied samples, except at low doping $n < 2 \times 10^{12}$ cm^{-2}, as expected. Indeed, $n \approx 2 \times 10^{12}$ cm^{-2} corresponds approximately to the threshold gate voltage,V_c, and to a Fermi level at the band edge in the simulations, i.e. the onset of the metallic regime. This observation is consistent with the presence of a tail of the DoS in the gap, and thermal broadening (*i.e.* thermal activation) which makes the actual band carrier concentration more poorly defined.

For a finer analysis, Figures 7(b-d) show the fitted experimental conductivities for the three devices. The defect density is $n_D = 1.7 \times 10^{12}$, 2.4×10^{12}, 3×10^{12} cm^{-2} for devices M1, M2 and M3 respectively. One can generally obtain an excellent fit for limited windows of carrier concentrations. However, as evidenced for M1 in particular, it can be challenging to find a single point-charge density that works well over a large range of concentrations, which shows the limitations of the effective point-charge model for the impurities. The corresponding values of impurity density cannot be directly related to the defect densities observed by Raman spectroscopy. Notably, the Raman methodology relies on the intensity of the LA(M) modes[28], likely linked to impurities with short-range scattering, while the transport model here accounts only for long-range Coulomb scattering. While both could come from the same kind of impurities (i.e. sulfur vacancies), their relative strength may vary with the experimental conditions, and there could also be other independent contributions to either short- or long-range scattering. We note that the agreement is fairly good for M1 (Raman estimation is $n_D \sim 1.5 - 3 \times 10^{12}$ cm^{-2}), while the discrepancy in M3 is clear (Raman estimation is $n_D < 2.5 \times 10^{11}$ cm^{-2}).

As seen in Figs 7(b-d), the simulations provide a very good fit to the slope of the temperature-dependent conductivity above $n = 3 \cdot 10^{12}$, which depends mostly on intrinsic mechanisms: phonon-scattering and screening. Phonon scattering is suppressed at low temperature, leaving charged impurity screening as the main mechanism in play to explain the doping dependency. The highest mobilities are thus reached at low temperature and high carrier densities. For the highest achievable doping in device M1 ($n \simeq 5 \times 10^{12}$ cm^{-2}), the conductivity reaches $\sigma \simeq 160$ μS at low temperatures, which corresponds to a mobility around $\mu_{\text{eff}} = 180$ cm^2/Vs.

Finally, while we can successfully apply the scaling theory suggesting a quantum phase transition below 100 K, we can not rule out the possibility of this being a classical phonon-related phenomena (following the 2D screening work by Das Sarma[36]). In particular, in the temperature range considered in this model, we see that the crossover can be understood by the combination of (i) the increase in the mobility (phonon related) and (ii) a change in carrier concentration with temperature, due to thermal activation of carriers, as discussed earlier and by Fang *et al.*[37]

V. CONCLUSION

To conclude, we have developed a method to anneal *in situ* MoS_2 devices before electrical measurements. This allowed us to obtain (almost always) good ohmic contacts at low temperatures, and to measure precisely the conductivity and mobility via four-probes measurements. The measured effective mobility is among the largest obtained in CVD-grown MoS_2 monolayer devices (with a maximum of ~ 180 cm^2/Vs at low temperature). When the Fermi energy is tuned in the tail of the conduction band, conductivity is driven by Efros-Schklovkii variable range hopping, with a universal and constant hopping prefactor, that is a clear indication that hopping is not phonon-mediated. Increasing electron density, an apparent MIT is observed. The possibility of a genuine 2D MIT cannot be ruled out, as we can observe a clear power-law diverging localization length close to the transition, and a one-parameter scaling can be realized. Whatever the case, at even higher carrier density, but not too low temperatures, the conductivity is well modeled by the Boltzmann equation for a non-interacting Fermi gas, taking into account both phonon and impurity scattering.

Acknowledgements

I.C. and S.N. acknowledge the Agence Nationale de la Recherche through the project JJEDi, ANR-18-CE24-0004. I.C, B.J and S.N. thank warmly M. Antezza and E. Baudin for fruitful discussions. T.S. and M.J.V. acknowledge simulation time awarded by PRACE (Optospin project id. 2020225411) on MareNostrum at the Barcelona Supercomputing Center". M.J.V. acknowledges ARC project DREAMS (G.A. 21/25-11) funded by Federation Wallonie Bruxelles and ULiege.

[1] S. Manzeli, D. Ovchinnikov, D. Pasquier, O. V. Yazyev, and A. Kis, Nature Review Materials **2**, 17033 (2017).
[2] H. Qiu, T. Xu, Z. Wang, W. Ren, H. Nan, Z. Ni, Q. Chen, S. Yuan, F. Miao, F. Song, et al., Nature Communications **4**, 2642 (2013).
[3] S.-C. Lu and J.-P. Leburton, Nanoscale Research Letters **9**, 676 (2014).
[4] K. F. Mak, C. Lee, J. Hone, J. Shan, and T. F. Heinz, Physical Review Letters **105**, 136805 (2010).
[5] W. Shi, J. Ye, Y. Zhang, R. Suzuki, M. Yoshida, J. Miyazaki, N. Inoue, Y. Saito, and Y. Iwasa, Scientific Reports **5**, 12534 (2015).
[6] N. Li, Q. Wang, C. Shen, Z. Wei, H. Yu, J. Zhao, X. Lu, G. Wang, C. He, L. Xie, et al., Nature Electronics **3**, 711 (2020).
[7] E. Singh, P. Singh, K. S. Kim, G. Y. Yeom, and H. S.

Nalwa, ACS Applied Materials & Interfaces **11**, 11061 (2019).
[8] B. Radisavljevic and A. Kis, Nature Materials **12**, 815 (2013).
[9] W. Zhu, T. Low, Y.-H. Lee, H. Wang, D. B. Farmer, J. Kong, F. Xia, and P. Avouris, Nature Communications **5**, 3087 (2014).
[10] Z. Yu, Y. Pan, Y. Shen, Z. Wang, Z.-Y. Ong, T. Xu, R. Xin, L. Pan, B. Wang, L. Sun, et al., Nature Communications **5**, 5290 (2014).
[11] H. Schmidt, S. Wang, L. Chu, M. Toh, R. Kumar, W. Zhao, A. H. Castro Neto, J. Martin, S. Adam, B. Özyilmaz, et al., Nano Letters **14**, 1909 (2014).
[12] R. Yang, X. Zheng, Z. Wang, C. Miller, and P. Feng, Journal of Vacuum Science and Technology B:Nanotechnology and Microelectronics **32**, 061203 (2014).
[13] D. Jariwala, V. K. Sangwan, D. J. Late, J. E. Johns, V. P. Dravid, T. J. Marks, L. J. Lauhon, and M. C. Hersam, Applied Physics Letters **102**, 173107 (2013).
[14] F. Ahmed, M. S. Choi, X. Liu, and W. J. Yoo, Nanoscale **7**, 9222 (2015).
[15] Y. Yoon, K. Ganapathi, and S. Salahuddin, Nano Letters **11**, 3768 (2011).
[16] B. W. H. Baugher, H. O. H. Churchill, Y. Yang, and P. Jarillo-Herrero, Nano Letters **13**, 4212 (2013).
[17] N. Huo, Y. Yang, Y.-N. Wu, X.-G. Zhang, S. T. Pantelides, and G. Konstantatos, Nanoscale **10**, 15071 (2018).
[18] T. Sohier, D. Campi, N. Marzari, and M. Gibertini, Physical Review Materials **2**, 114010 (2018).
[19] S. M. Gali, A. Pershin, A. Lherbier, J.-C. Charlier, and D. Beljonne, The Journal of Physical Chemistry C **124**, 15076 (2020).
[20] D. Lembke, A. Allain, and A. Kis, Nanoscale **7**, 6255 (2015).
[21] J. M. Lu, O. Zheliuk, I. Leermakers, N. F. Q. Yuan, U. Zeitler, K. T. Law, and J. T. Ye, Science **350**, 1353 (2015).
[22] J. T. Ye, Y. J. Zhang, R. Akashi, M. S. Bahramy, R. Arita, and Y. Iwasa, Science **338**, 1193 (2012).
[23] B. H. Moon, J. J. Bae, M.-K. Joo, H. Choi, G. H. Han, H. Lim, and Y. H. Lee, Nature Communications **9**, 2052 (2018).
[24] B. H. Moon, G. H. Han, M. M. Radonjić, H. Ji, and V. Dobrosavljević, Physical Review B **102**, 245424 (2020).
[25] B. H. Moon, Emergent Materials **4**, 989 (2021).
[26] C. Lee, H. Yan, L. E. Brus, T. F. Heinz, J. Hone, and S. Ryu, ACS Nano **4**, 2695 (2010).
[27] G. L. Frey, R. Tenne, M. J. Matthews, M. S. Dresselhaus, and G. Dresselhaus, Physical Review B **60**, 2883 (1999).
[28] S. Mignuzzi, A. J. Pollard, N. Bonini, B. Brennan, I. S. Gilmore, M. A. Pimenta, D. Richards, and D. Roy, Physical Review B **91**, 195411 (2015).
[29] D. Ovchinnikov, A. Allain, Y.-S. Huang, D. Dumcenco, and A. Kis, ACS Nano **8**, 8174 (2014).
[30] J.-R. Chen, P. M. Odenthal, A. G. Swartz, G. C. Floyd, H. Wen, K. Y. Luo, and R. K. Kawakami, Nano Letters **13**, 3106 (2013).
[31] Y. Pan, J. Gu, H. Tang, X. Zhang, J. Li, B. Shi, J. Yang, H. Zhang, J. Yan, S. Liu, et al., ACS Applied Nano Materials **2**, 4717 (2019).
[32] G. He, H. Ramamoorthy, C. P. Kwan, Y. H. Lee, J. Nathawat, R. Somphonsane, M. Matsunaga, A. Higuchi, T. Yamanaka, N. Aoki, et al., Nano Letters **16**, 6445 (2016).
[33] N. Kaushik, D. M. Mackenzie, K. Thakar, N. Goyal, B. Mukherjee, P. Boggild, D. H. Petersen, and S. Lodha, npj 2D Materials and Applications **1**, 1 (2017).
[34] J. Shu, G. Wu, Y. Guo, B. Liu, X. Wei, and Q. Chen, Nanoscale **8**, 3049 (2016).
[35] X. Chen, Z. Zhou, B. Deng, Z. Wu, F. Xia, Y. Cao, L. Zhang, W. Huang, N. Wang, and L. Wang, Nano Today **27**, 99 (2019).
[36] S. D. Sarma, E. H. Hwang, and Q. Li, Physical Review B **88**, 155310 (2013).
[37] N. Fang and K. Nagashio, Journal of Physics D: Applied Physics **51**, 065110 (2018).
[38] E. Abrahams, P. W. Anderson, D. C. Licciardello, and T. V. Ramakrishnan, Physical Review Letters **42**, 673 (1979).
[39] S. D. Sarma and E. H. Hwang, Physical Review B **89**, 235423 (2014).
[40] H. V. Phuc, N. N. Hieu, B. D. Hoi, N. V. Hieu, T. V. Thu, N. M. Hung, V. V. Ilyasov, N. A. Poklonski, and C. V. Nguyen, Journal of Electronic Materials **47**, 730 (2018).
[41] H. Shi, H. Pan, Y.-W. Zhang, and B. I. Yakobson, Physical Review B **87**, 155304 (2013).
[42] L. V. Keldysh, Soviet Journal of Experimental and Theoretical Physics Letters **29**, 658 (1979).
[43] M. Salmani-Jelodar, Y. Tan, and G. Klimeck, in *2011 International Semiconductor Device Research Symposium (ISDRS)* (IEEE, 2011).
[44] J. Xue, S. Huang, J.-Y. Wang, and H. Q. Xu, RSC Advances **9**, 17885 (2019).
[45] S. Ghatak, A. N. Pal, and A. Ghosh, ACS Nano **5**, 7707 (2011).
[46] K. Bennaceur, P. Jacques, F. Portier, P. Roche, and D. C. Glattli, Physical Review B **86**, 085433 (2012).
[47] M. Furlan, Physical Review B **57**, 14818 (1998).
[48] F. W. V. Keuls, X. L. Hu, H. W. Jiang, and A. J. Dahm, Physical Review B **56**, 1161 (1997).
[49] W. Mason, S. V. Kravchenko, G. E. Bowker, and J. E. Furneaux, Physical Review B **52**, 7857 (1995).
[50] I. Shlimak, K.-J. Friedland, and S. Baranovskii, Solid State Communications **112**, 21 (1999).
[51] S. I. Khondaker, I. S. Shlimak, J. T. Nicholls, M. Pepper, and D. A. Ritchie, Physical Review B **59**, 4580 (1999).
[52] M. P. Sarachik and P. Dai, Europhysics Letters (EPL) **59**, 100 (2002).
[53] A. L. Efros and M. Pollak, *Electron-Electron Interactions in Disordered Systems* (De Gruyter, Berlin, Boston, 1986), pp. 497–498.
[54] L. Fleishman, D. C. Licciardello, and P. W. Anderson, Physical Review Letters **40**, 1340 (1978).
[55] I. L. Aleiner and B. I. Shklovskii, Physical Review B **49**, 13721 (1994).
[56] R. Berkovits and B. I. Shklovskii, Journal of Physics: Condensed Matter **11**, 779 (1999).
[57] V. Kozub, S. Baranovskii, and I. Shlimak, Solid State Communications **113**, 587 (2000).
[58] N. Papadopoulos, G. A. Steele, and H. S. J. van der Zant, Physical Review B **96**, 235436 (2017).
[59] A. Zabodskii and A. Andreev, International Journal of Modern Physics B **08**, 883 (1994).
[60] A. Pérez-Garrido, M. Ortuño, E. Cuevas, J. Ruiz, and M. Pollak, Physical Review B **55**, R8630 (1997).
[61] S. Das Sarma and E. H. Hwang, Scientific Reports **5**, 16655 (2015).
[62] N. R. Pradhan, A. McCreary, D. Rhodes, Z. Lu, S. Feng,

E. Manousakis, D. Smirnov, R. Namburu, M. Dubey, A. R. H. Walker, et al., Nano Letters **15**, 8377 (2015).

[63] T. Sohier, P. M. M. C. de Melo, Z. Zanolli, and M. J. Verstraete, arXiv p. 2207.00452 (2022).

[64] P. Giannozzi, S. Baroni, N. Bonini, M. Calandra, R. Car, C. Cavazzoni, D. Ceresoli, G. L. Chiarotti, M. Cococcioni, I. Dabo, et al., Journal of Physics: Condensed Matter **21**, 395502 (2009).

[65] P. Giannozzi, O. Andreussi, T. Brumme, O. Bunau, M. Buongiorno Nardelli, M. Calandra, R. Car, C. Cavazzoni, D. Ceresoli, M. Cococcioni, et al., Journal of Physics Condensed Matter **29**, 465901 (2017).

[66] T. Sohier, M. Calandra, and F. Mauri, Physical Review B **96**, 075448 (2017).

[67] K. Kaasbjerg, T. Low, and A.-P. Jauho, Physical Review B **100**, 115409 (2019).

[68] T. Sohier, M. Gibertini, and M. J. Verstraete, Physical Review Materials **5**, 024004 (2021).